Dust temperature tracing the ISRF intensity in the Galaxy

Journal Item

A&A 518, L88 (2010)
DOI: 10.1051/0004-6361/201014540

Astronomy & Astrophysics
Special feature

Herschel: the first science highlights

Letter to the Editor

Dust temperature tracing the ISRF intensity in the Galaxy⋆,⋆⋆

J.-Ph. Bernard[1,2], D. Paradis[3], D. J. Marshall[1,2], L. Montier[1,2], G. Lagache[4], R. Paladini[3], M. Veneziani[5], C. M. Brunt[6], J. C. Mottram[6], P. Martin[7,8], I. Ristorcelli[1,2], A. Noriega-Crespo[3], M. Compiègne[7], N. Flagey[3], L. D. Anderson[9], C. C. Popescu[10], R. Tuffs[11], W. Reach[3], G. White[12,13], M. Benedetti[14], L. Calzoletti[15], A. M. DiGiorgio[14], F. Faustini[15], M. Juvela[16,17], C. Joblin[1,2], G. Joncas[18], M.-A. Mivilles-Deschenes[4], L. Olmi[19,20], A. Traficante[21], F. Piacentini[5], A. Zavagno[9], and S. Molinari[14]

(Affiliations are available in the online edition)

Received 30 March 2010 / Accepted 26 April 2010

ABSTRACT

New observations with *Herschel* allow accurate measurement of the equilibrium temperature of large dust grains heated by the interstellar radiation field (ISRF), which is critical in deriving dust column density and masses. We present temperature maps derived from the *Herschel* SPIRE and PACS data in two fields along the Galactic plane, obtained as part of the Hi-GAL survey during the *Herschel* science demonstration phase (SDP). We analyze the distribution of the dust temperature spatially, as well as along the two lines-of-sight (LOS) through the Galaxy. The zero-level offsets in the *Herschel* maps were established by comparison with the IRAS and *Planck* data at comparable wavelengths. We derive maps of the dust temperature and optical depth by adjusting a detailed model for dust emission at each pixel. The dust temperature maps show variations in the ISRF intensity and reveal the intricate mixture of the warm dust heated by massive stars and the cold filamentary structures of embedded molecular clouds. The dust optical depth at 250 μm is well correlated with the gas column density, but with a significantly higher dust emissivity than in the solar neighborhood. We correlate the optical depth with 3-D cubes of the dust extinction to investigate variations in the ISRF strength and dust abundance along the line of sight through the spiral structure of the Galaxy. We show that the warmest dust along the LOS is located in the spiral arms of the Galaxy, and we quantify their respective IR contribution.

Key words. ISM: general – dust, extinction – ISM: clouds – galaxies: ISM – infrared: ISM – submillimeter: ISM

1. Introduction

The far-infrared (FIR) emission of the Galaxy is dominated by emission from the largest dust grains (BG: big grains) in the interstellar medium (ISM) with sizes around 0.1 μm. In the diffuse ISM, these grains radiate in thermal equilibrium and their temperature is set by the balance between cooling through IR emission and heating through absorption of the visible (VIS) and ultraviolet (UV) photons of the interstellar radiation field (ISRF). Since the absorption of BGs is reasonably flat over the VIS-UV range, their temperature is largely independent of the hardness of the ISRF. Spatial variations in the dust equilibrium temperature therefore trace spatial variations in the integrated ISRF strength, referred to as $X_{\rm ISRF}$. Measuring variations in $X_{\rm ISRF}$ is important for dust mass determination, but also for quantifying photodissociation at the surface of molecular clouds. Variations in the dust temperature can also be used to identify the densest regions within molecular clouds, independent of molecular tracers. They can also reflect changes in the dust optical properties, if the nature of dust changes significantly.

Previous FIR observations of the diffuse ISM at high and intermediate Galactic latitude with the IRAS, DIRBE, and FIRAS instruments have established that the average dust equilibrium temperature in the solar neighborhood is about 17.5 K (Boulanger et al. 1996; Lagache et al. 1998) assuming a dust emissivity index of $\beta = 2$. Towards brighter regions along the Galactic plane, the derived dust temperature maps clearly indicate the presence of colder dust in the outer regions of the Galaxy, at about 13 K and warmer dust in the inner regions (e.g. Reach et al. 1995; Lagache et al. 1998), as well as in nearby star-forming regions (Ophiuchi, Orion), at about 20 K. Such large-scale investigations were clearly limited by the lack of angular resolution (typically 1° for DIRBE). Balloon-borne experiments operating in the FIR have revealed the spatial distribution of dust temperature on arc-minute scales in several star-forming regions (Dupac et al. 2001; Ristorcelli et al. 1998) and more diffuse environments (Bernard et al. 1999). These observations showed apparent dust temperatures as low as $T_{\rm D} \simeq 13$ K towards molecular regions, going down to $T_{\rm D} \simeq 11$ K in dense regions, after subtraction of the emission from the surrounding warmer background. They also showed, through the unexpected decrease in the dust temperature in some translucent molecular clouds, an increase in the dust emissivity, which was interpreted as the aggregation of dust into fractal clusters (Stepnik et al. 2003; Paradis et al. 2009). These early observations, however, lacked the large-scale coverage required for a meaningful statistical analysis. *Herschel* now offers the possibility of deriving such temperature maps at sub-arcmin resolution on large scales.

⋆ *Herschel* is an ESA space observatory with science instruments provided by European-led Principal Investigator consortia and with important participation from NASA.

⋆⋆ Figures 3–6 are only available in electronic form at http://www.aanda.org

In this paper, we construct the first dust temperature maps of the Galactic plane from the *Herschel* data. The maps are used to derive the distribution of the total dust optical depth at 250 μm and to explore its correlation with the total gas column density. We perform a preliminary exploration of the distribution of the dust emission along the LOS through correlation with differential extinction measurements.

2. Gains and offsets

The processing of the Hi-GAL data and map making are described in Molinari et al. (2010). We converted the maps from Jy/beam and Jy/pix (for SPIRE and PACS, respectively) into MJy/sr using the conversion factors given in Table 1. For PACS, these were also divided by the recommended factors of 1.05 and 1.29 (PACS 70 and 160 μm, respectively) to match the point-source calibration on standard stars and asteroids. For SPIRE, they correspond to the most up-to-date estimate of the beam area to be used for extended emission (M. Ferlet, private communication). At this early stage of the *Herschel* data analysis, we have adopted gain uncertainties of ±20%.

As for most bolometer observations without an absolute calibrator, the zero level (or offset) of the PACS and SPIRE Hi-GAL data is unknown. This is a problem in particular for deriving the dust temperature, since arbitrary offsets in the various photometric bands would lead to erroneous SEDs and temperature. This is usually addressed through background subtraction, but such an approach is inaproppriate for the large-scale analysis of the Hi-GAL data, since the data only extends 1° off the Galactic plane, and there is strong emission up to the map boundaries. To derive the offsets in our maps, we took advantage of the fact that the *Planck* satellite has 2 common photometric channels with SPIRE at 857 GHz (350 μm) and 545 GHz (550 μm). In these bands, the *Planck*-HFI data are calibrated with respect to FIRAS (Piat et al. 2002). *Planck* has already observed a large fraction of the sky, covering the two Hi-GAL SDP fields, which allow us to set a proper zero level. The offsets have not yet been computed in the current *Planck* pipeline (V3.1), so were evaluated by the *Planck* Core-Team for the purpose of this work, to match the FIR-HI correlation at intermediate Galactic latitudes in the lowest column density regions of the sky, based on the HI Dwingeloo Survey (Hartmann 1996). We estimate the accuracy of the offset determination to better than 5%. The offset-corrected *Planck* data of the Hi-GAL SDP fields at 857 GHz and 545 GHz were then combined with the IRIS data (Miville-Deschênes et al. 2005) at 100 μm, to produce values of the expected total flux in the SPIRE 500 and 350 μm filters, and were provided to us (*Planck* Core-Team, private communication). Frequency interpolation and color correction in the *Planck*, IRAS, and *Herschel* filters were performed using the DUSTEM model (e.g. Compiègne et al. in prep., Bernard et al. 2008) with the radiation field intensity set to match the *Planck* and the IRIS 100 μm data at 5′ resolution. We then smoothed the Hi-GAL maps to the common *Planck* HFI resolution of 5′ and compared the integrated emission in the Hi-GAL fields to the predictions of the *Planck*-IRIS estimates derived above. The offset in each channel (see Table 1) were derived as the difference between the two. As expected, they are higher for the $l = 30°$ field, which is toward brighter regions of the inner Galaxy.

Table 1. PACS pixel and SPIRE beam areas and offsets (MJy/sr) used in this paper.

	PACS		SPIRE		
λ (μm)	70	160	250	350	500
area ($''^2$)	10.24	20.25	395.0	740.0	1571.0
$l = 30°$	688.0	1982.3	1042.0	462.2	170.9
$l = 59°$	60.9	395.7	292.0	150.9	61.4

3. Dust temperature and opacity maps

The offset-corrected Hi-GAL SDP data were used to produce maps of the dust temperature according to the following procedure. We first used the DUSTEM code to produce a precalculated table of the expected brightness in the *Herschel* SPIRE and PACS filters for various values of the ISRF intensity scaling factor $X_{\rm ISRF}$. This calculation assumed the standard dust composition proposed by Désert et al. (1990). It includes proper color correction in all PACS and SPIRE photometric channels. The spectral shape of the ISRF used is similar to that of Mathis et al. (1983) for a galactrocentric distance of 10 kpc, although with an integral from 0.09 to 8 μm lower by a factor 0.81. The Hi-GAL maps were smoothed to the common resolution of the SPIRE 500 μm channel (36.9″) through convolution with a Gaussian kernel with the appropriate width. The pre-calculated table was then used to minimize the χ^2 between the model predictions and the observed brightness distribution of each pixel of the map, leading to the best estimate of the $X_{\rm ISRF}$ factor for each pixel. The dust temperature of the BG was then derived using $T_{\rm D} = 17.5\ {\rm K}(X_{\rm ISRF})^{1/(4+\beta)}$, which relies on the determination by Boulanger et al. (1996) for the solar neighborhood. We used a fixed dust emissivity index of $\beta = 2$, which is consistent with the findings of Boulanger et al. (1996) over the spectral range of the Hi-GAL data and with the assumption of the DUSTEM code for each grain size. As a large fraction of the dust emission at 70 μm is produced by small grains experiencing thermal fluctuations, we did not consider the PACS 70 μm channel when deriving the temperature. After experimenting with using several combinations of the remaining Hi-GAL channels, it appeared that including the PACS 160 μm produced artifacts in the temperature maps. This is likely caused by improper correction of low level stripes in the data and/or poorly determined gains for this channel. We therefore decided to restrict the determination to the SPIRE channels and used all 3 channels at 250, 350, and 500 μm to derive the temperature maps. The method described above relies on a more physical modeling than the use of a simple gray body fit, in the sense that it accounts for the effect of a grain size distribution. However, we checked that the $T_{\rm D}$ values differ only marginally from those given by a gray-body fit with $\beta = 2$ for the range of temperatures sampled here. With the adopted gain errors of ±20%, the maximum uncertainty on $T_{\rm D}$ ranges from ±1.5 K at $T_{\rm D} = 13$ K to ±2.5 K at $T_{\rm D} = 20$ K.

The dust temperature maps and histograms obtained for the two fields are shown in Fig. 1. In Table 2, we give average values ($\widetilde{T_{\rm D}}$) and compare them with the average temperatures derived from DIRBE data for the same fields by Lagache et al. (1998). The inner SDP field at $l = 30°$ clearly shows higher temperatures than the outer field at $l = 59°$. This is not surprising since the dust temperature maps of Lagache et al. (1998) showed this gradient from inner to outer Galaxy regions on large scales. The average temperatures derived here for the two fields agree with the DIRBE ones to within 0.7 K and 0.3 K, which is within the combined uncertainties. The temperature maps of both fields show coherent variations that trace the fluctuations of the ISRF intensity caused both by the presence of localized heating sources and ISRF attenuation in density structures.

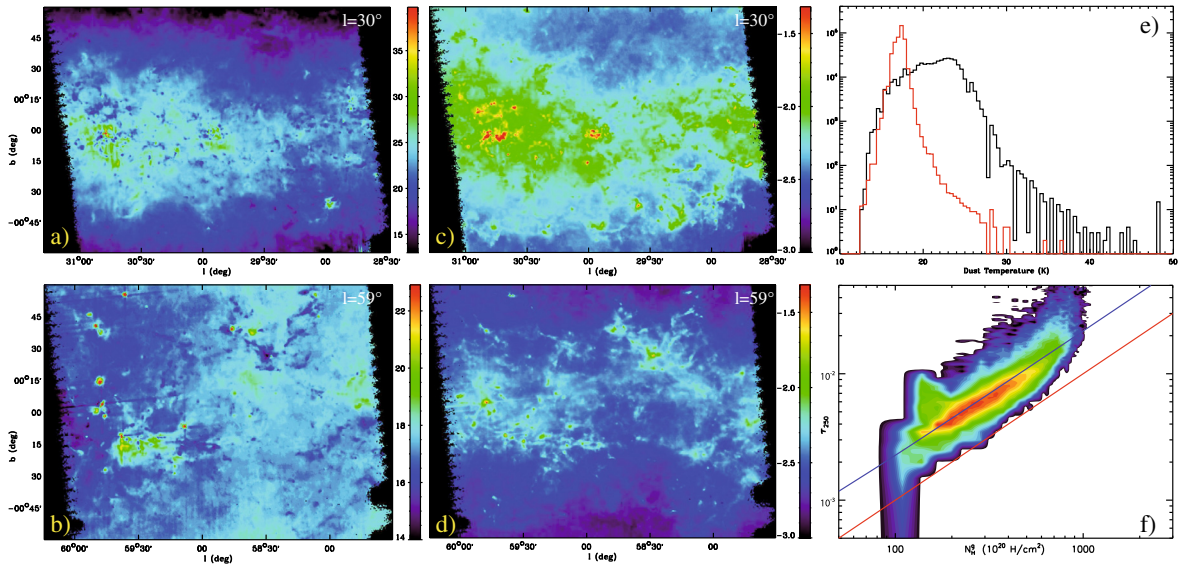

Fig. 1. a), **b)**: temperature maps for the $l = 30°$ and $l = 59°$ fields; **c)**, **d)**: τ_{250} maps for the $l = 30°$ and $l = 59°$ fields, in log scale; **e)**: temperature histograms for the $l = 30°$ (black) and $l = 59°$ (red) fields; **f)**: correlation between τ_{250} and the total gas column density for the $l = 30°$ field. The red line shows $\tau_{250}/N_{\rm H} = 10^{-25}$ cm^2. The blue line shows the best fit obtained (see text). Panels **a)**–**d)** are also available as online material.

Table 2. Average $\widetilde{T}_{\rm D}$ in the SDP fields and best-fit parameters for different regions along the LOS (see text for details).

Field	$l = 30°$				$l = 59°$		
$\widetilde{T}_{\rm D}^{\rm DIRBE\dagger}$	20.6 K ($X_{\rm ISRF} = 2.6$)				17.9 K ($X_{\rm ISRF} = 1.1$)		
$\widetilde{T}_{\rm D}^{\rm Hi-GAL}$	21.3 K ($X_{\rm ISRF} = 3.3$)				18.2 K ($X_{\rm ISRF} = 1.3$)		
Region[b]	Sag.	Scu.1	Scu.2	Dif.	Vul.	Per.	Dif.
$T_{\rm D}$ (K)	24.5	19.7	24.1	18.9	17.1	18.8	14.3
$\Delta T_{\rm D}$ (K)	±1.0	±0.7	±1.0	±0.6	±0.5	±0.6	±0.3
$\tau_{250}/N_{\rm H}$[‡]	5.0	11.3	5.8	10.0	1.9	2.7	4.2

Notes. [(†)] Averaged over $2° \times 2°$ in the maps of Lagache et al. (1998). [(b)] Sag. = Sagittarius (0–2.5 kpc), Scu=Scutum-Crux (3.5–6, 6–8 kpc), dif = diffuse, Vul = Vulpecula (0–3.5 kpc), Per = Perseus (6–10 kpc). [(‡)] In 10^{-25} cm^2.

Comparison with the ^{13}CO ($J = 1$–0) GRS data cube (Jackson et al. 2006) in the $l = 30°$ field and of the ^{13}CO data of Brunt et al. (in prep.) in the $l = 59°$ field shows that the many cold spots in both maps often correspond to structures or edges of molecular structures. They are organized along aligned winding structures, indicating that they belong to large-scale filamentary structures of the ISM. Their typical sizes range from a few arcmin to several tens of arcminutes. Their temperature is $\simeq$13 K, corresponding to $X_{\rm ISRF} \simeq 0.17$. Compared to the surrounding warmer material at $\simeq$20 K ($X_{\rm ISRF} \simeq 2.6$), this suggests an attenuation factor in these structures of at least 15, corresponding to structures with edge-to-center extinction of at least 3 mag (total $A_V > 6$ mag assuming spherical geometry). This is a lower limit since apparent dust temperature overestimates the actual physical temperature, owing to warmer foreground and background emission. The lowest apparent temperatures measured here are consistent with those derived from earlier FIR observations in the same wavelength range using balloon-borne experiments towards both diffuse and star-forming regions (e.g. Bernard et al. 1999; Dupac et al. 2001). We have noticed that, in the $l = 30°$ field, the SPIRE intensity maps used in the temperature determination actually reach negative values in low brightness regions at $|b| > 1°$, despite adding the offsets. This could be the result of uncertain gain calibration of the data, which may also explain why $T_{\rm D}$ is correlated with intensity in this field, which has the broadest intensity dynamical range. We suspect that the low $T_{\rm D}$ values near map edges may be affected. To avoid these regions, the temperature histograms shown in Fig. 1 have been computed in the region with $|b| < 0.9°$.

Using the temperature maps derived above, we constructed the dust optical depth map at 250 μm (see Fig. 1) as $\tau_{250} = I_{250}/B_\nu(T_{\rm D})$. We also constructed maps of the total gas column density using the VGPS HI (Stil et al. 2006) and the ^{13}CO($J = 1$–0) data. The neutral gas column density was derived from the HI integrated intensity $W_{\rm HI}$ in K km s^{-1} using $N_{\rm H}^g = 1.82 \times 10^{18} W_{\rm HI}$. The molecular column density $N_{\rm H}^{\rm CO}$ was derived using Eqs. (1) and (2) of Dobashi et al. (1994), with an excitation temperature $T_{\rm ex} = 10$ K and assuming $N_{\rm H} = 2 * N_{\rm H_2}$. The best correlation between τ_{250} and $N_{\rm H}^g = N_{\rm H}^{\rm HI} + N_{\rm H}^{\rm CO}$ is found to be $\tau_{250}/N_{\rm H}^g = 2.2 \times 10^{-25}$ cm^2 and 3.6×10^{-25} cm^2 for the $l = 30°$ (see Fig. 1) and $l = 59°$ fields respectively. These are a few times higher than the canonical value of $\tau_{250}/N_{\rm H} = 10^{-25}$ cm^2 by Boulanger et al. (1996) for the solar neighborhood. We used the ^{12}CO($J = 1$–0) maps from Brunt et al. (in prep.) ($l = 59°$) and Sanders et al. (2003) ($l = 30°$) to compute the intensity weighted excitation temperature over the two fields and found values consistent with the assumed one, which excludes the $T_{\rm ex}$ values (typically 24 K) that would be required to reconcile these values. Similarly, invoking the uncertainty on $T_{\rm D}$ would require that $T_{\rm D}$ values are overestimated by 6 K, which is unlikely. Because the dust emission is dominated by the molecular component in those fields, this result could indicate that we are seeing an increased emissivity due to grain aggregation. Alternative explanations include a higher dust/gas ratio in the plane, a larger contribution of gas not traced by HI or CO (such as H_2 with no CO) as in the solar neighborhood or large departure from the optically thin assumption for the HI emission.

4. Line-of-sight mixing

The temperature maps we derived result from the mixing of various dust excitation conditions along the LOS. Toward $l = 30°$, and referring to the spiral arm model of Vallée (2008), we expect the main contributions from the Sagittarius ($d = 2.5$ kpc, $d = 12$ kpc), the tangent point of the Scuttum-Crux ($d = 6$–8.5 kpc) and the Perseus ($d = 13.5$ kpc) arms. For the field $l = 59°$,

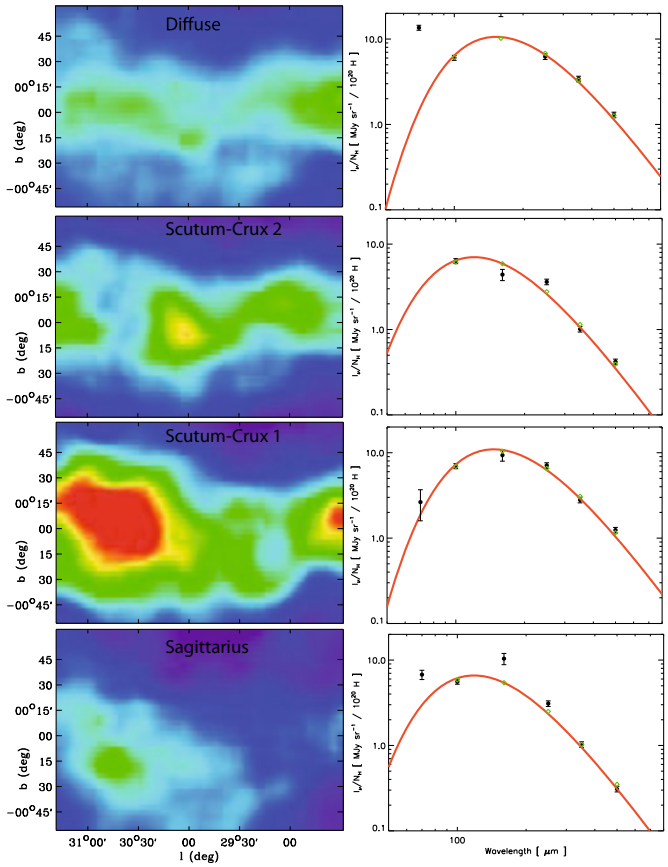

Fig. 2. *Left*: integrated H column density in the various distance bins toward the $l = 30°$ field derived from differential extinction. The log-scale color table goes from 0 to 2.5×10^{22} H/cm^2. *Right*: SEDs of the emission correlated to each bin. The fit shown is for a gray body with $\beta = 2$. The green symbols are the predictions of the model in the filters. The fitted values are given in Table 2.

we expect contributions from the Vulpecula star formation region ($d \sim 2$ kpc) and the Perseus arm ($d = 8.5$ kpc). Searching for such variations is recognized as a complicated inversion problem. In the past, this has been addressed mainly by using Galactic inversion techniques (see e.g. Paladini et al. 2007) where the gas tracers (mainly HI, CO and radio data) are used with a Galactic rotation curve to construct spatial templates at various Galactocentric distances. The IR emission is then correlated against those templates to infer dust properties as a function of Galactocentric radius. However, these methods do not currently allow us to derive the spatial variations associated with the spiral structure of the Galaxy.

Here, we illustrate a different approach that is independent of a kinematic model of the Milky Way. We used the genetic forward modeling presented by Marshall et al. (2009) to construct a 3-D distribution of the interstellar extinction toward the two SDP fields. This was done using the Besançon stellar model (Robin et al. 2003), along with infrared stellar observations from 2MASS (Skrutskie et al. 2006) and GLIMPSE (Benjamin et al. 2003). This technique produces a cube of the extinction as a function of distance from the sun. The extinction cubes were divided into a number of spatial templates: for the $l = 30°$ field, one corresponding to the Sagittarius arm, two to the Scutum-Crux arm as well as one containing the remaining, diffuse extinction. For the $l = 59°$ field, the templates correspond to Vulpecula, the Perseus arm, and the diffuse extinction. The IR data, including the IRIS 100 μm, which was degraded to the same angular resolution as the extinction (5′), were then correlated against the resulting spatial templates. The resulting dust emission parameters are given in Table 2. They show a tendency toward significantly warmer dust in regions of the LOS such as the intersection with spiral arms, where star-forming regions presumably dominate the emission. Consistent with the result of the correlation with the gas, the dust emissivity derived is higher than the local value for the $l = 59°$ field. The even higher values for the $l = 30°$ field probably reveal that extinction does not trace the full amount of dust along this crowded LOS.

5. Conclusions

We derived maps of the equilibrium temperature of large dust grains in the two Galactic fields covered by the Hi-GAL SDP data at the resolution of 36.9″. The maps trace the spatial variations in the integrated ISRF intensity. The two fields show an intricate mixture of varying temperatures. Many cold spots are identified, which likely correspond to dense regions within molecular clouds. Some may actually host pre-stellar cores. The lowest temperatures observed are ≃13 K, which would occur in shielded regions where starlight is less than 17% of the diffuse interstellar radiation field at the solar circle. The highest temperatures observed are of ≃40−50 K and are likely to correspond to PDRs and HII regions. We constructed maps of the dust optical depth at 250 μm and examined the correlation with total gas column density. We find a $\tau_{250}/N_{\rm H}$ ratio 2−3 times higher than the canonical solar neighborhood value, similar to findings from earlier balloon-borne experiments in the same spectral range. This may reflect a large contribution from dust aggregates in molecular regions. We used newly determined LOS density derivations from extinction and attempted a first inversion of the Hi-GAL data. We showed that dust is warmer in the star- forming regions in Galactic arms than in the diffuse component.

Acknowledgements. We acknowledge the *Planck* consortium for allowing the use of the *Planck* HFI data for propagating the zero level to the SPIRE bands.

References

Benjamin, R. A., Churchwell, E., Babler, B. L., et al. 2003, PASP, 115, 953
Bernard, J. P., Abergel, A., Ristorcelli, I., et al. 1999, A&A, 347, 640
Bernard, J.-Ph., Reach, W. T., Paradis, D., et al. 2008, AJ, 136, 919
Boulanger, F., Abergel, A., Bernard, J.-P., et al. 1996, A&A, 312, 256
Désert, F.-X., Boulanger, F., & Puget, J. L. 1990, A&A, 237, 215
Dobashi, K., Bernard, J. P., Yonekura, Y., et al. 1994, ApJS, 95,419
Dupac, X., Giard, M., Bernard, J.-P., et al. 2001, ApJ, 553, 604
Hartmann, D., & Burton, W. B. 1996, Atlas of Galactic Neutral Hydrogen (Cambridge University Press)
Jackson, J. M., Rathborne, J. M., Shah, R. Y., et al. 2006, ApJS, 163, 145
Lagache, G., Abergel, A., Boulanger, F., & Puget, J. L. 1998, A&A, 333, 709
Mathis, J. S., Mezger, P. G., & Panagia, N. 1983, A&A, 128, 212
Marshall, D. J., Joncas, G., & Jones, A. P. 2009, ApJ, 706, 727
Miville-Deschênes, M.-A., & Lagache, G. 2005, ApJS, 157, 302
Molinari, S., et al. 2010, A&A, 518, L100
Paladini, R., Montier, L., Giard, M., et al. 2007, A&A, 465, 839
Paradis, D., Bernard, J.-Ph., & Mény, C. 2009, A&A, 506, 745
Piat, M., Lagache, G., Bernard, J. P., et al. 2002, A&A, 393, 359
Reach, W. T., Dwek, E., Fixsen, D. J., et al. 1995, ApJ, 451, 188
Ristorcelli, I., Serra, G., Lamarre, J. M., et al. 1998, ApJ, 496, 267
Robin, A. C., Reylé, C., Derrière, S., & Picaud, S. 2003, A&A, 409, 523
Sanders, D. B., Clemens, D. P., Scoville, N. Z., et al. 1986, ApJS, 60, 1
Skrutskie, M. F., Cutri, R. M., Stiening, R., et al. 2006, AJ, 131, 1163
Stepnik, B., Abergel, A., Bernard, J.-P., et al. 2003, 2003, A&A, 398, 551
Stil, J. M., Taylor, A. R., Dickey, J. M., et al. 2006, AJ, 132, 1158
Vallée, J. P. 2008, AJ, 135, 1301

Pages 5 to 9 are available in the electronic edition of the journal at http://www.aanda.org

[1] Université de Toulouse, UPS, CESR, 9 avenue du colonel Roche, 31028 Toulouse Cedex 4, France
e-mail: Jean-Philippe.Bernard@cesr.fr
[2] CNRS, UMR5187, 31028 Toulouse, France
[3] Spitzer Science Center, California Institute of Technology, CALTECH, 1200 East California Boulevard, MC 220-6, Pasadena, CA 91125, USA
[4] Institut d'Astrophysique Spatiale, Université Paris XI, 91405 Orsay, France
[5] Dipartimento di Fisica, Università di Roma 1 "La Sapienza", Roma, Italy
[6] University of Exeter, Physics Building, Stocker Road, Exeter EX4 4QL, UK
[7] Canadian Institute for Theoretical Astrophysics, University of Toronto, 60 St. George Street, Toronto, ON M5S 3H8, Canada
[8] Department of Astronomy & Astrophysics, University of Toronto, 50 St. George Street, Toronto, ON M5S 3H4, Canada
[9] Laboratoire d'Astrophysique de Marseille (UMR 6110 CNRS & Université de Provence), 38 rue F. Joliot-Curie, 13388 Marseille Cedex 13, France
[10] Jeremiah Horrocks Institute, University of Central Lancashire, Preston PR1 2HE, UK
[11] Max Planck Institut f"ur Kernphysik, Saupfercheckweg 1, 69117 Heidelberg, Germany
[12] The Rutherford Appleton Laboratory, Chilton, Didcot OX11 0NL, UK
[13] Department of Physics & Astronomy, The Open University, Milton Keynes MK7 6AA, UK
[14] INAF-IFSI - via Fosso del Cavaliere 100, Rome, Italy
[15] ASI Science Data Center, 00044 Frascati (Rome), Italy
[16] Observatory, University of Helsinki, Finland
[17] Departement de Physique, Université Laval, Québec, Canada
[18] Department of Physics, 00014, University of Helsinki, Finland
[19] INAF, Osservatorio Astrofisico di Arcetri, Largo E. Fermi 5, 50125, Firenze, Italy
[20] University of Puerto Rico, Rio Piedras Campus, Physics Dept., Box 23343, UPR station, San Juan, Puerto Rico, USA
[21] Dipartimento di Fisica, Università di Roma 2 "Tor Vergata", Rome, Italy

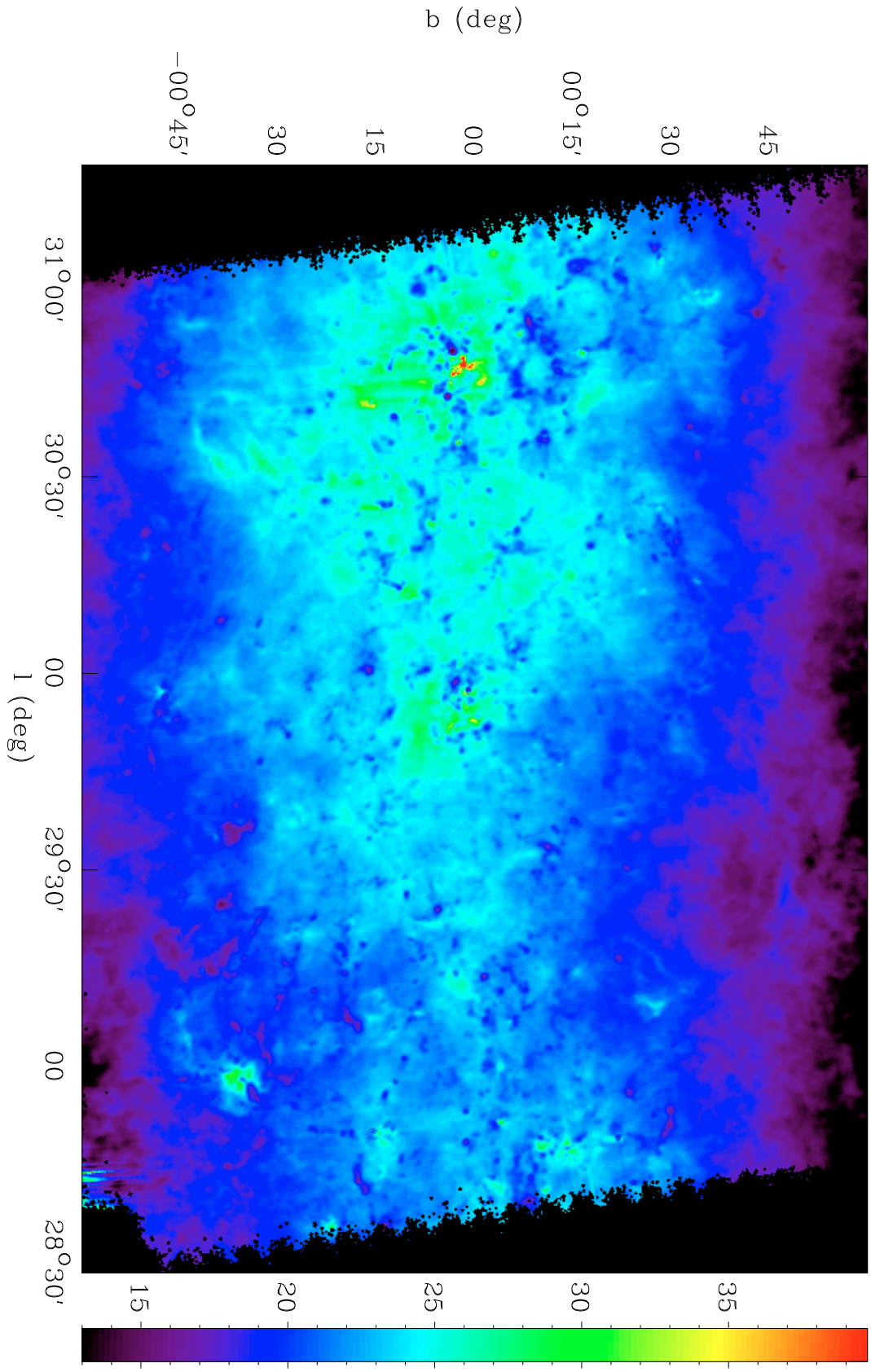

Fig. 3. Temperature map (Fig. 1a) for the field $l = 30°$.

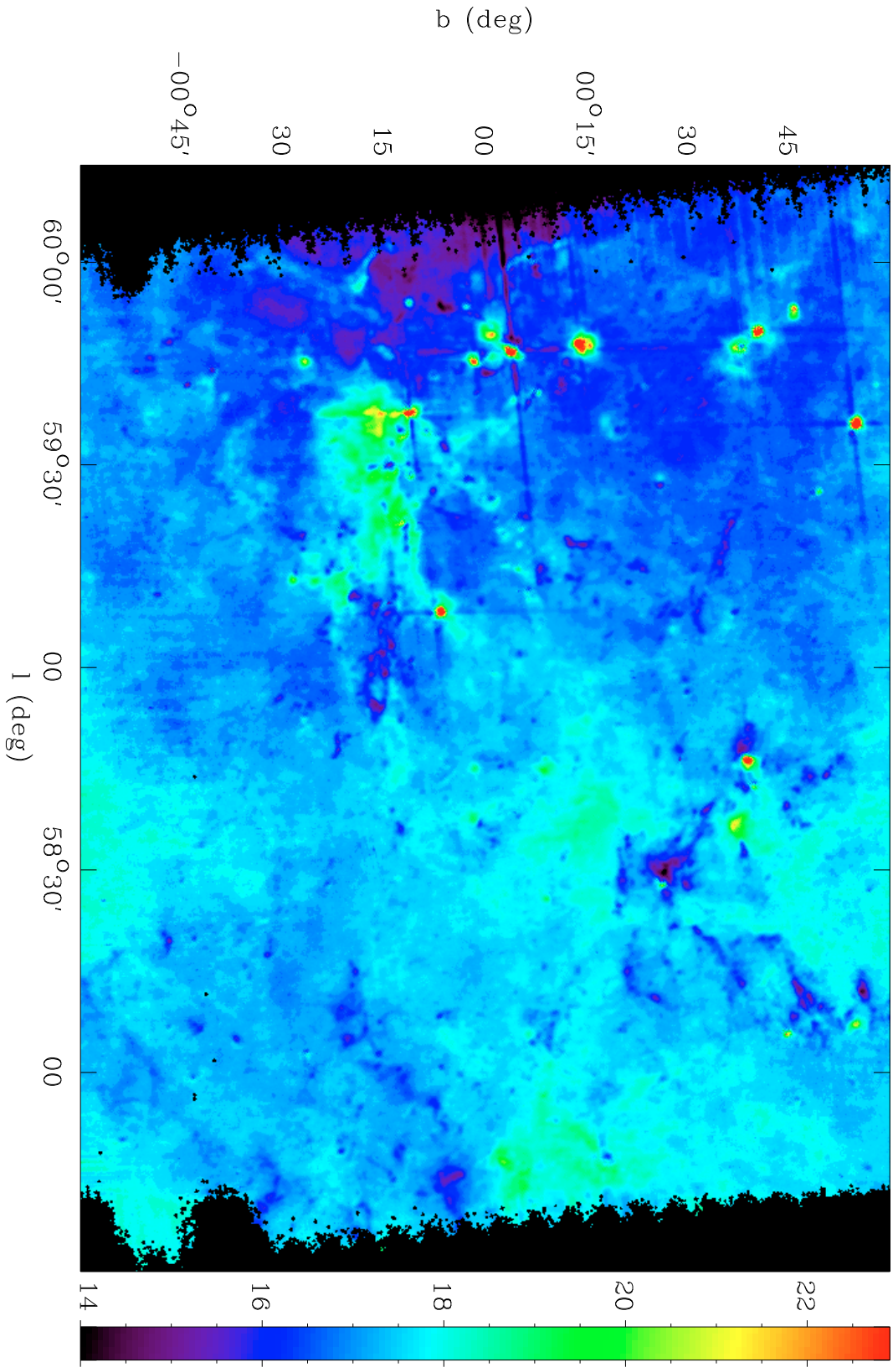

Fig. 4. Temperature map (Fig. 1b) for the field $l = 59°$.

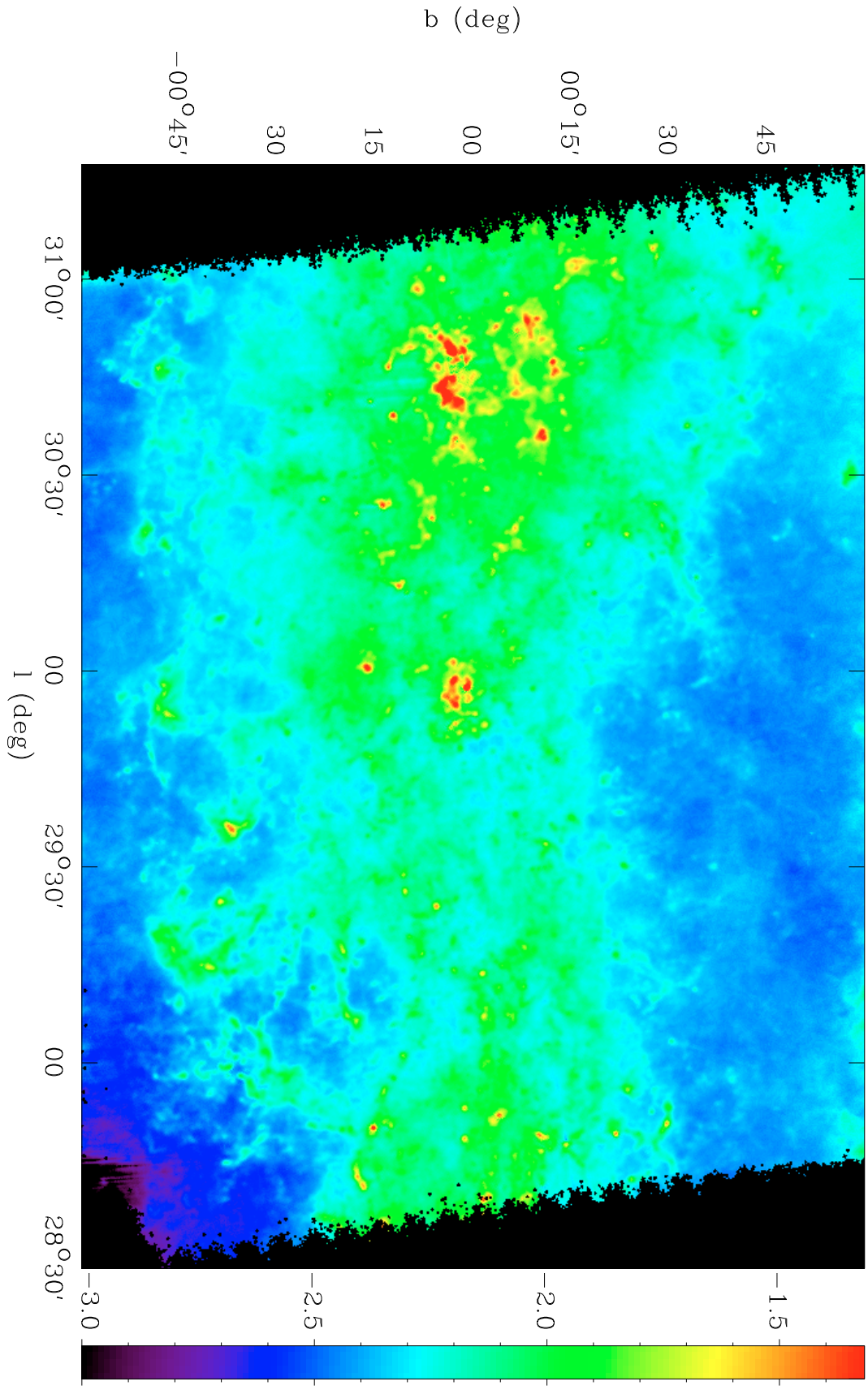

Fig. 5. 250 μm optical depth (Fig. 1c) for the field $l = 30°$.

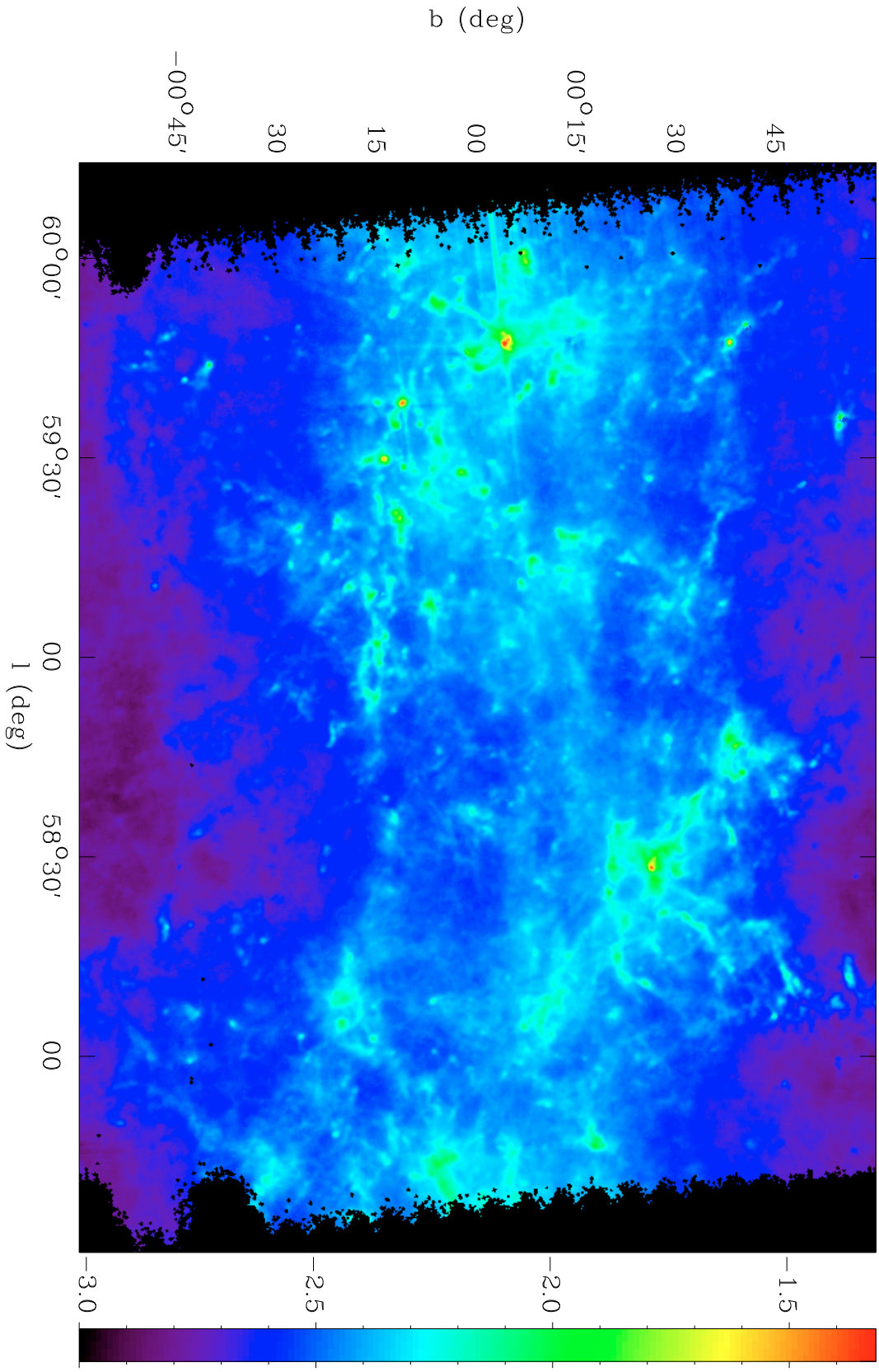

Fig. 6. 250 μm optical depth (Fig. 1d) for the field l = 59°.